Optimization of Chemical Exchange Saturation Transfer (CEST) Parameters at 7 Tesla for Validation of GAG- and APT-CEST Measurements of Fibroglandular Tissue of the Breast

Adrienne N. Dula, Ph.D.[1,2], **Blake E. Dewey, B.S.**[1], **Lori R. Arlinghaus, Ph.D.**[1], **Jason M. Williams, Ph.D.**[1], **Dennis Klomp, Ph.D.**[1,3], **Thomas E. Yankeelov, Ph.D.**[1,2,4,5,6,7,8], and **Seth Smith, Ph.D.**[1,2,4,5,6]

[1]Institute of Imaging Science, Vanderbilt University, Nashville, Tennessee, USA [2]Department of Radiology and Radiological Sciences, Vanderbilt University, Nashville, Tennessee, USA [3]Department of Radiology, University Medical Center Utrecht, The Netherlands [4]Program in Chemical and Physical Biology, Vanderbilt University, Nashville, Tennessee, USA [5]Biomedical Engineering, Vanderbilt University, Nashville, Tennessee, USA [6]Physics and Astronomy, Vanderbilt University, Nashville, Tennessee, USA [7]Cancer Biology, Vanderbilt University, Nashville, Tennessee, USA [8]Vanderbilt Ingram Cancer Center, Vanderbilt University, Nashville, Tennessee, USA

Abstract

Purpose—The two purposes of this study were to: 1) implement simulation-optimized chemical exchange saturation transfer (CEST) measurements sensitive to amide proton transfer (APT) and glycosaminoglycans (GAG) hydroxyl proton transfer effects in the human breast at 7 Tesla, and 2) determine the reliability of these techniques for evaluation of fibroglandular tissue in the healthy breast as a benchmark for future studies of pathology.

Materials and Methods—All human studies were IRB approved, HIPPA compliant, and included informed consent. The CEST parameters of saturation duration (25 ms) and amplitude (1 μT) were chosen based on simulation-driven optimization for APT contrast with the CEST effect quantified using residuals of a Lorentzian fit. Optimized parameters were implemented at 7 Tesla in ten healthy women in two separate scans to evaluate the reliability of CEST MRI measurements in the breast. CEST *z*-spectra were acquired over saturation offset frequencies ranging between ±40 ppm using a quadrature unilateral breast coil. The scan-rescan reliability was assessed in terms of the intraclass correlation coefficient, which indicates the ratio of between-subject variation to total variation.

Results—Simulations of the Bloch Equations with chemical exchange guided selection of optimal values for pulse duration and amplitude, 25 ms and 1 μT, respectively. Reliability was

Please address correspondence to: Adrienne Dula, Ph.D., Vanderbilt University Institute of Imaging Science, Vanderbilt University Medical Center, AA-1105 Medical Center North, 1161 21st Avenue South, Nashville, Tennessee 37232-2310, Phone: (615) 343-0471, Fax: (615) 322-0734, adrienne.n.dula@vanderbilt.edu.

Implications for patient care: None

evaluated using intraclass correlation coefficients (95% confidence intervals) with acceptable results: 0.963 (0.852, 0.991) and 0.903 (0.609, 0.976) for *APT* and *GAG*, respectively.

Conclusion—We used simulations to derive optimal CEST preparation parameters to elicit maximal CEST contrast in healthy fibroglandular breast tissue due to APT at 7 T. We demonstrate that by using these parameters, obtaining reproducible values for both the amide and hydroxyl protons from of CEST MRI at 7 T is feasible in the human breast

Introduction

As tumors undergo a myriad of chemical changes, the metabolic byproducts may be indirectly measured with chemical exchange saturation transfer (CEST) MRI using endogenous metabolite sensitivity enhancement through exchange with water protons (1). The sensitivity of CEST to these subtle chemical changes may provide complementary biomarkers of pathology to conventional (T_1- and T_2-weighted) MRI while providing fundamentally different information than established quantitative techniques.

CEST MRI uses the transfer of saturation to study mobile compounds within tissue by selectively saturating labile protons such as those residing in amide bonds of proteins/peptides (amide proton transfer [APT]) and hydroxyl moieties using narrow-bandwidth radio frequency (RF) irradiation. This saturation is transferred to bulk water causing the water signal to be slightly attenuated. The resulting water signal is observed as a function of saturation frequency relative to water, termed the *z*-spectrum (2), because the water pool is much larger than the saturated solute proton pool, each exchanging saturated solute proton is replaced by a non-saturated water proton, which is then again saturated. This results in signal enhancement and allows the presence of low-concentration solutes to be examined indirectly. CEST has been used to examine cancer in brain (3) and breast (4–6), detecting increased APT in tumor due to differences in pH and protein content inside cells. This sensitivity to intracellular protein content provides valuable information regarding the viability and health of fibroglandular tissue. The increased APT signal found in tumors has been attributed to an increase in free protein concentration in malignant cells (3, 7, 8). While APT has been studied in a myriad of oncology applications, hydroxyl exchange represents a largely unexplored area particularly in breast where glycosaminoglycan (GAG) content could be an important indicator of tissue status. As active mediators in cell-cell and cell-matrix interactions, proteoglycans significantly affect neoplastic cell behavior (9) with increased proteoglycan content found in mammary tumors (10).

While access to APT moieties can be obtained at lower field strengths, the hydroxyl protons of GAG are less accessible due to their rapid exchange rate and proximity to the water resonance. There have been no prior studies of CEST targeted at hydroxyl protons performed at lower fields such as 1.5 T or 3.0 T (11, 12). These previously inaccessible protons can be studied at 7.0 T due to increased chemical dispersion, facilitating selective saturation, decreasing pulse bandwidth demands, and a favorable exchange regime. Additionally, higher field strength translates to higher achievable resolution, better anatomical coverage, or a decreased imaging time. Our goal was to optimize CEST acquisition and analysis to minimize and characterize variability in CEST-derived APT and

hydroxyl proton transfer (derived from GAG) measurements in the healthy fibroglandular breast tissue at 7 T.

Materials and Methods

All human studies were IRB approved, HIPPA compliant, and included informed consent. Data were obtained using a whole body 7 T Philips Achieva scanner (Philips Medical Systems, Cleveland, OH).

Simulations

Theoretical saturation was modeled according to the Bloch equations (13) with transfer effects modified for steady-state and time-dependent magnetization for CEST (14) to optimize preparation (RF irradiation power and bandwidth) for chemical exchange occurring around 3.5 ppm (APT CEST) and 1.5 ppm (GAG CEST) downfield from water in healthy breast tissue at 7 T using MATLAB 2012b (Mathworks, Natick, MA). The magnetization profile at a frequency offset from water, defined by ω, was studied using the matrix solution (14) in a three-pool model (15) including 1) a labile, slow exchange resonance (CEST) centered at $\omega = 3.5$ ppm and 1.5 ppm for APT and GAG, respectively, 2) a direct water saturation component at $\omega = 0$ ppm, and 3) an asymmetric magnetization transfer (MT) component centered at $\omega = -2.34$ ppm. We examined the effects of varying saturation parameters on APT and hydroxyl resonances, which were calculated by integrating the CEST effect between 3.0 – 4.0 ppm and 1.0 – 2.0 ppm, respectively.

The saturation pulse power (B_1 amplitude) was modeled as a 30 ms single-lobed sinc-Gauss pulse from 1 μT to 3 μT. Next, B_1 amplitude was fixed to 1 μT while pulse duration was varied from 0 ms – 60 ms. A 3D pulsed-CEST approach (16) was chosen using a single RF irradiation every T_R, creating a cumulative saturation effect and building up steady state over multiple short T_R's. Physical constants included: 1) water protons: $T_1 = 2.3$ s and $T_2 = 45$ ms, 2) amide protons: $T_1 = 1.0$ s, $T_2 = 20$ ms, and $k_{ex} = 50$ s^{-1}, 3) hydroxyl protons: $T_1 = 1.0$ s, $T_2 = 40$ ms, and $k_{ex} = 500$ s^{-1}, and 4) MT: $T_1 = 1.6$ s, $T_2 = 0.001$ ms, and $k_{ex} = 20$ s^{-1} (5, 17).

Subjects

Ten women (median age: 24, range: 22 – 33) with no history of breast disease underwent two MRI examinations occurring within two weeks (median: 4 days, range: 1–14 days).

MR Imaging

A local transmit/receive breast coil (18) was used for unilateral RF transmission/reception (MR Coils BV, Drunen, the Netherlands).

CEST data were acquired using a 3D gradient echo, multi-shot sequence (6 shots). Fat suppression included a water-selective binomial excitation pulse train with an interpulse separation of 0.5 ms to allow a short echo time, T_E, of 2.7 ms. The dynamic scan time was 10.2 seconds and T_R was 20.0 ms. The acquisition matrix was $152 \times 152 \times 12$ over a 150 mm $\times$ 150 mm $\times$ 72 mm field of view. The nominal excitation was 3.6°, the estimated Ernst

angle for glandular tissue at 7 T based on the previously published T_1 (17) and prescribed T_R.

Saturation was achieved using a 25 ms, 1 µT sinc-Gauss pulse applied at forty-four saturation-offset frequencies (ω) between ±40 ppm with saturation far off resonance ($\omega = 80$ ppm) acquired twice at the beginning of the sequence, once at the end, and interleaved ever five acquisitions, resulting in a total of 56 dynamics. The proximity of the breast to the lungs creates a time-dependent B_0 field fluctuation, which can be de-convolved from the overall CEST effect by calculating time-varying S_0 (see Data Analysis) (19).

Data Analysis

Image co-registration used a non-rigid 3D affine transformation (20). The healthy fibroglandular (FG) tissue was isolated using a semi-automated segmentation as previously described (4). The signal intensities ($S(\omega)$) from images acquired with saturation far off resonance were defined as $S_0 = S(\omega = 80$ ppm). The S_0 images were fit to a cubic spline as a function of time to calculate the z-spectrum $= S(\omega)/S_0$ based on acquisition time. To correct for field inhomogeneities, points of the z-spectrum selected to exclude the resonances of interest for APT and GAG (5 ppm $< \omega < 1$ ppm) were fit to a single Lorentzian and the minima was assigned to the water frequency ($\omega = 0$ ppm). The CEST effect was calculated as the integrated area between the Lorentzian fit and z-spectrum, expressed as $CEST_{Lor}$ for amide proton transfer (APT_{Lor}) associated with proteins and peptides (21) where 3.0 ppm $< \omega < 4.0$ ppm and hydroxyl protons associated with glycosaminoglycans (GAG_{Lor}, termed gagCEST) where 1.0 ppm $< \omega < 2.0$ ppm (22).

Statistical Analysis

Statistical analyses were performed using SPSS R19 (IBM, Armonk, New York). Scan-rescan CEST-derived indices for APT_{Lor} and GAG_{Lor} were compared in two ways. Bland-Altman analysis determined variability between mean values of the two scans for each subject (n = 10) (23) with the mean difference evaluated against the limits of agreement (LOA). Importantly, if the 95% confidence interval for the mean difference includes zero, this supports the null hypothesis that there is no scan-rescan difference ($\alpha = 0.05$). The scan-rescan reliability was assessed in terms of the intraclass correlation coefficient (ICC) (24) according to Eq. [1]:

$$reliability = \frac{between\ subjects\ variability}{between\ subjects\ variability + error}. \quad [1]$$

The ICC-derived reliability indicates the ratio of between-subject variation to total variation; *i.e.*, it is the sum of within- and between-variation using mean squared values derived from within subject repeated-measures ANOVA. With this, we can establish the threshold for a measured difference to be biophysical rather than measurement noise.

Results

Simulations

Simulation results for both APT (Panel A) and GAG (Panel B) are displayed in Figure 1. $CEST_{Lor}$ is shown as a function of pulse duration and amplitude, with maximum APT contrast found for pulse amplitudes of 0.5 μT – 1.5 μT within the pulse duration range of 15 – 40 ms. Importantly, this range of saturation amplitudes and durations corresponds to a maximum for both APT and GAG CEST and, therefore, saturation pulse parameters were chosen as 25 ms duration with 1.0 μT amplitude to capture both resonances.

MR Imaging

Example test-retest data are shown in Figure 2; Panel A presents an S_0 image, $\omega = 80$ ppm, Panel B presents the APT_{Lor} map calculated at 3 ppm $< \omega < 4$ ppm, and Panel C presents the GAG_{Lor} map calculated at 1 ppm $< \omega < 2$ ppm. The time-variation of S_0 data is seen in Figure 3A with S_0 signal intensity of masked FG tissue shown as a function of acquisition time (black dots) with the calculated spline fit (black line). Example z-spectra calculated using the uncorrected, mean value of twelve S_0 images (gray line) and de-trended z-spectra (black line) are shown in Panel B. The non-corrected data show large deviations around the APT resonance and signal variations due to nuclear Overhauser enhancement (NOE) (25), observed in previous studies of gagCEST (22). De-trending minimizes influence from up-field resonances, but CEST effects around 3.5 and 1.5 ppm (APT and GAG, respectively) remain. Cohort-wise CEST results are shown in Figure 4. Panel A depicts the mean z-spectra derived from masked FG tissue of all data (solid black line) (n = 10 subjects, two scans each), and inter-scan standard deviation represented by dashed gray lines. These results can be examined on a voxel-by-voxel basis where calculated APT_{Lor} (Panel B) and GAG_{Lor} (Panel C) for each of the ten healthy subjects' scans are shown side-by-side for comparison of the mean (solid black line) and the standard deviations (dashed gray line). Panel A demonstrates overall inter-subject repeatability, while Panels B and C indicate that the mean and standard deviation were comparable for each subject's repeated measures.

Statistical Analysis

Bland-Altman plots are shown in Figure 5 with subject-wise differences plotted against the mean value for each subjects' APT_{Lor} (Panel A) and GAG_{Lor} measurements (Panel B). Using the calculated standard error of the mean (SEM) (0.45 % for APT_{Lor} and 0.17 % for GAG_{Lor}), mean differences were 0.41 % for APT_{Lor} and 0.61 % for GAG_{Lor} (indicated by the solid black lines), neither of which were significantly different from zero. The LOA were (–2.54 %, 3.45 %) for APT_{Lor}, and (–2.06 %, 2.77 %) for GAG_{Lor}, (α = 0.05) and are indicated by the dotted lines in Figure 5. Using Eq. [2], the reliability of mean values was 2.93 and 2.53 for APT_{Lor} and GAG_{Lor}, respectively. The resulting ICC (95% CIs) for average measures of APT_{Lor} was 0.963 (0.852, 0.991) and 0.903 (0.609, 0.976) for GAG_{Lor}.

Discussion

This study presents optimization of acquisition parameters, a processing technique to simultaneously study the CEST effect for two resonances (APT and GAG) of interest in the

breast, and evaluation of reliability in healthy FG tissue *in vivo* at 7 T. The method for quantification of the CEST effect can have large impact on calculated indices, particularly reproducibility. The scan-rescan reliability values (2.93 for the APT_{Lor} and 2.35 for the GAG_{Lor}) can be interpreted as the noise-to-signal ratio (i.e., the inverse of the signal-to-noise, SNR); however, this metric is also sensitive to both systematic and random variation between the scan-rescan events (26). We extended test-retest analyses to include the ICC with the resulting ICC values for both APT and GAG CEST being greater than 0.9, indicating strong agreement between scans as well as their potential value in future clinical studies.

Given the sample size (n = 10) of this initial study, it is difficult to control for age and menstrual cycle effects, which are known to modulate breast tissue density and composition (27). Further studies will include intra-scan registration to account for such effects. Additionally, the ICC is a composite measure precluding isolation of specific sources of variability. Finally, future simulations will explore attainable contrast to noise for expected pathological changes in CEST effects.

The current standard of care for MRI examination of breast disease involves 1.5 T evaluation of morphometric changes and contrast agent distribution based on MR images, providing non-specific assessment of tumor characteristics. We leveraged increased field strength to provide reliable quantitative metabolic information non-invasively with the potential to detect tissue abnormalities by establishing the clinically relevant difference for detection of pathology. Through evaluation of variability in healthy glandular tissue, it is possible to define a change in measured CEST effect that is clinically significant which is important for future diagnostic and prognostic studies. Thus, the potential for high field CEST MRI in the breast is substantial and is important as the ability to assess resonances that may play a key role in understanding breast disease cannot be captured by alternative or lower magnetic field techniques.

Acknowledgments

References

1. Goffeney N, Bulte JW, Duyn J, Bryant LH Jr, van Zijl PC. Sensitive NMR detection of cationic-polymer-based gene delivery systems using saturation transfer via proton exchange. J Am Chem Soc. 2001; 123(35):8628–9. [PubMed: 11525684]

2. Ward KM, Aletras AH, Balaban RS. A new class of contrast agents for MRI based on proton chemical exchange dependent saturation transfer (CEST). J Magn Reson. 2000; 143(1):79–87. [PubMed: 10698648]

3. Jones CK, Schlosser MJ, van Zijl PC, Pomper MG, Golay X, Zhou J. Amide proton transfer imaging of human brain tumors at 3T. Magn Reson Med. 2006; 56(3):585–92. [PubMed: 16892186]

4. Dula AN, Arlinghaus LR, Dortch RD, et al. Amide proton transfer imaging of the breast at 3 T: Establishing reproducibility and possible feasibility assessing chemotherapy response. Magn Reson Med. 2012

5. Schmitt B, Zamecnik P, Zaiss M, et al. A new contrast in MR mammography by means of chemical exchange saturation transfer (CEST) imaging at 3 Tesla: preliminary results. RoFo : Fortschritte auf

dem Gebiete der Rontgenstrahlen und der Nuklearmedizin. 2011; 183(11):1030–6. [PubMed: 22034086]

6. Klomp DW, Dula AN, Arlinghaus LR, et al. Amide proton transfer imaging of the human breast at 7T: development and reproducibility. NMR Biomed. 2013

7. Zhou J, Blakeley JO, Hua J, et al. Practical data acquisition method for human brain tumor amide proton transfer (APT) imaging. Magn Reson Med. 2008; 60(4):842–9. [PubMed: 18816868]

8. Zhou J, Lal B, Wilson DA, Laterra J, van Zijl PC. Amide proton transfer (APT) contrast for imaging of brain tumors. Magn Reson Med. 2003; 50(6):1120–6. [PubMed: 14648559]

9. Iozzo RV. Proteoglycans and neoplasia. Cancer metastasis reviews. 1988; 7(1):39–50. [PubMed: 3293831]

10. Alini M, Losa GA. Partial characterization of proteoglycans isolated from neoplastic and nonneoplastic human breast tissues. Cancer Res. 1991; 51(5):1443–7. [PubMed: 1997183]

11. Haris M, Cai K, Singh A, Hariharan H, Reddy R. In vivo mapping of brain myo-inositol. NeuroImage. 2011; 54(3):2079–85. [PubMed: 20951217]

12. van Zijl PC, Jones CK, Ren J, Malloy CR, Sherry AD. MRI detection of glycogen in vivo by using chemical exchange saturation transfer imaging (glycoCEST). Proc Natl Acad Sci U S A. 2007; 104(11):4359–64. [PubMed: 17360529]

13. Woessner DE. Nuclear transfer effects in nuclear magnetic resonance pulse experiments. The Journal of Chemical Physics. 1961; 35(1):41–8.

14. Woessner DE, Zhang S, Merritt ME, Sherry AD. Numerical solution of the Bloch equations provides insights into the optimum design of PARACEST agents for MRI. Magn Reson Med. 2005; 53(4):790–9. [PubMed: 15799055]

15. Desmond KL, Stanisz GJ. Understanding Quantitative Pulsed CEST in the Presence of MT. Magnetic Resonance in Medicine. 2012; 67(4):979–90. [PubMed: 21858864]

16. Jones CK, Polders D, Hua J, et al. In vivo three-dimensional whole-brain pulsed steady-state chemical exchange saturation transfer at 7 T. Magn Reson Med. 2012; 67(6):1579–89. [PubMed: 22083645]

17. Haddadin IS, McIntosh A, Meisamy S, et al. Metabolite quantification and high-field MRS in breast cancer. NMR Biomed. 2009; 22(1):65–76. [PubMed: 17957820]

18. Klomp DW, van de Bank BL, Raaijmakers A, et al. 31P MRSI and 1H MRS at 7 T: initial results in human breast cancer. NMR Biomed. 2011; 24(10):1337–42. [PubMed: 21433156]

19. Jones CK, Huang A, Xu J, et al. Nuclear Overhauser enhancement (NOE) imaging in the human brain at 7T. NeuroImage. 2013; 77:114–24. [PubMed: 23567889]

20. Netsch T, van Muiswinkel A. Quantitative evaluation of image-based distortion correction in diffusion tensor imaging. IEEE Trans Med Imaging. 2004; 23(7):789–98. [PubMed: 15250631]

21. Zhou JY, Payen JF, Wilson DA, Traystman RJ, van Zijl PCM. Using the amide proton signals of intracellular proteins and peptides to detect pH effects in MRI. Nat Med. 2003; 9(8):1085–90. [PubMed: 12872167]

22. Ling W, Regatte RR, Navon G, Jerschow A. Assessment of glycosaminoglycan concentration in vivo by chemical exchange-dependent saturation transfer (gagCEST). Proc Natl Acad Sci U S A. 2008; 105(7):2266–70. [PubMed: 18268341]

23. Bland JM, Altman DG. Statistical methods for assessing agreement between two methods of clinical measurement. Lancet. 1986; 1(8476):307–10. [PubMed: 2868172]

24. Koch, G. Intraclass correlation coefficient. In: Johnson, SKaNL., editor. Encyclopedia of Statistical Sciences. New York, NY: John Wiley & Sons; 1982. p. 213-7.

25. van Zijl PC, Zhou J, Mori N, Payen JF, Wilson D, Mori S. Mechanism of magnetization transfer during on-resonance water saturation. A new approach to detect mobile proteins, peptides, and lipids. Magn Reson Med. 2003; 49(3):440–9. [PubMed: 12594746]

26. Landman BA, Bazin PL, Smith SA, Prince JL. Robust estimation of spatially variable noise fields. Magn Reson Med. 2009; 62(2):500–9. [PubMed: 19526510]

27. de Lima CR, de Arimatea dos Santos J Junior, Nazario AC, Michelacci YM. Changes in glycosaminoglycans and proteoglycans of normal breast and fibroadenoma during the menstrual cycle. Biochimica et biophysica acta. 2012; 1820(7):1009–19. [PubMed: 22542782]

Advances in knowledge

1. This study provides optimal parameters and establishes reliability of 7 Tesla chemical exchange saturation transfer (CEST) MRI of the breast with intraclass correlation coefficients (95% confidence intervals) of: 0.963 (0.852, 0.991) and 0.903 (0.609, 0.976) for *APT* and *GAG*, respectively.

2. This study describes frequency drift correction for isolation of CEST effects.

3. This study establishes the clinically significant level of change for application of CEST MRI in breast pathology.
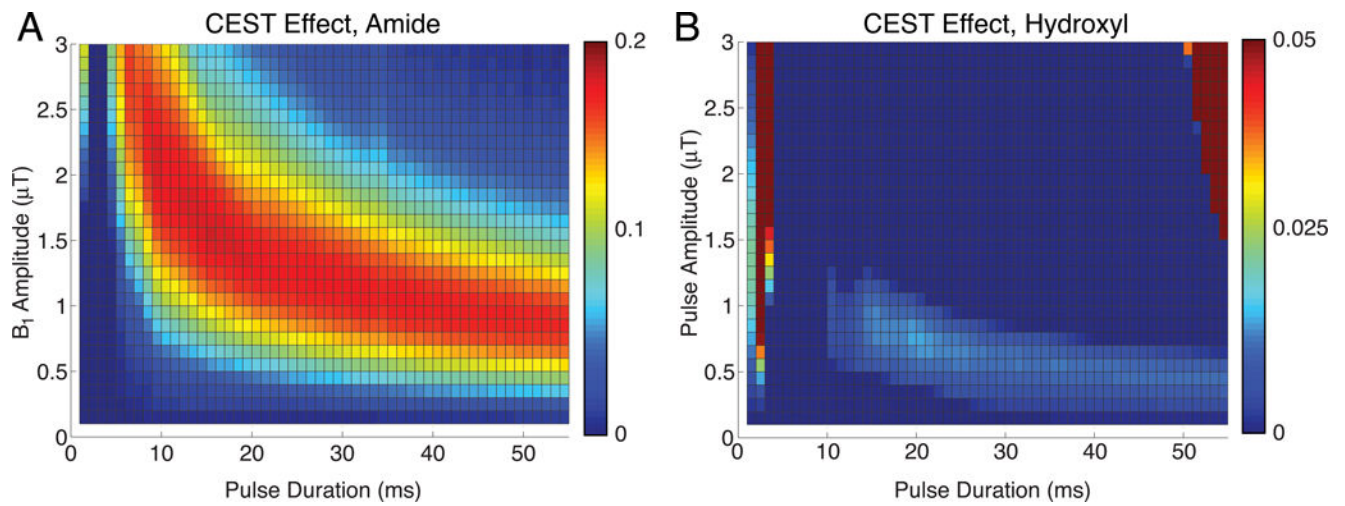
Figure 1.
Simulation of pulsed CEST MRI guiding saturation parameters with A) showing the APT CEST effect as a function of saturation pulse amplitude and duration. B) Choosing saturation parameters eliciting optimal APT and minimum scan time, hydroxyl proton exchange simulations indicate potential to detect this fast exchanging moiety as well.
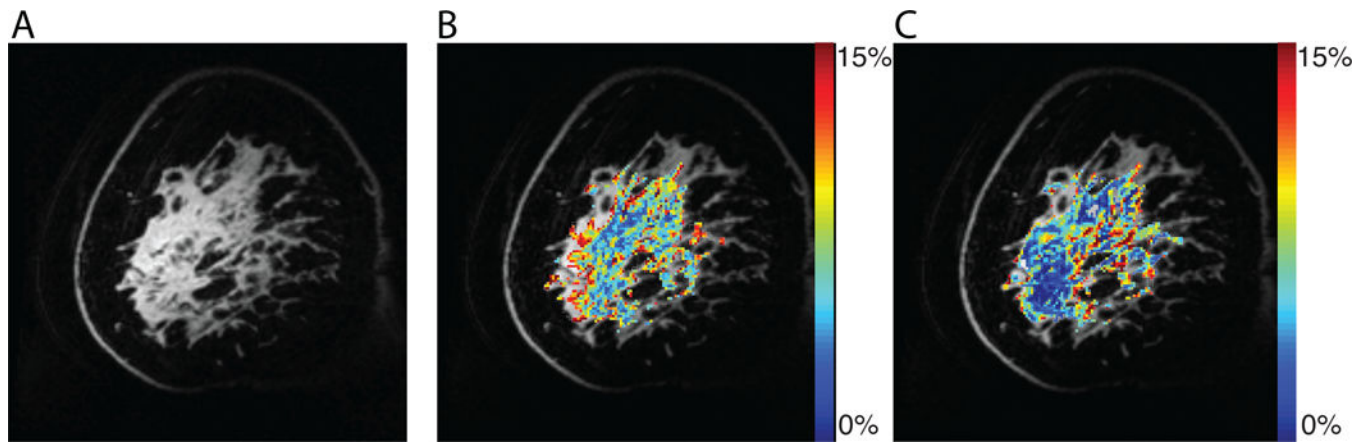
Figure 2.
Example images from CEST MRI data set. A) An S_0 image acquired with a saturation offset of 80 ppm provides anatomic detail. B) An APT map calculated using an image acquired following saturation at 3.5 ppm downfield from water depicting an increased amide exchange affect in anterior glandular tissue. C) A GAG map calculated using an image acquired 1.6 ppm downfield from water which is associated with hydroxyl protons
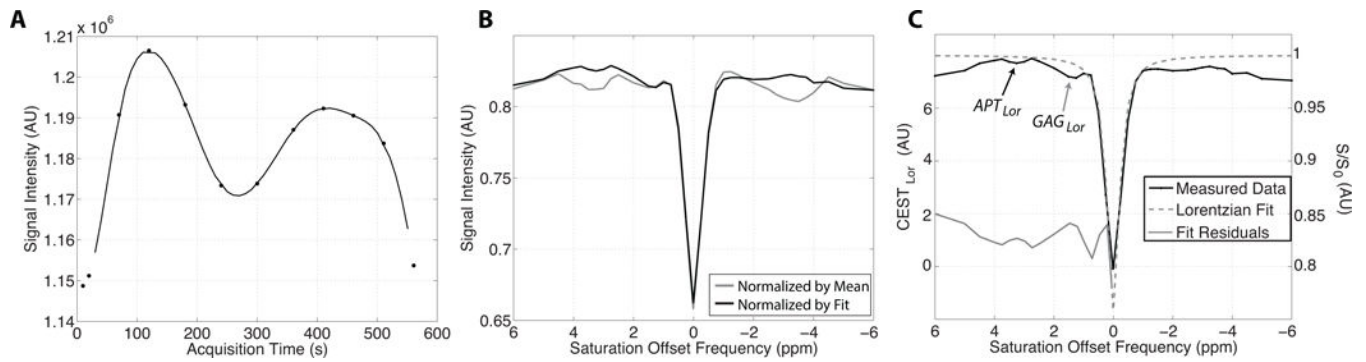
Figure 3.

Details of CEST MRI data acquisition and processing. A) Mean signal intensity of masked fibroglandular tissue in S_0 image volumes (black dots) acquired intermittently used for z-spectrum normalization, where ω= 80 ppm, plotted as a function of acquisition time. A cubic spline fit (black line) was used to extrapolate S_0 signal intensities. B) Example z-spectra normalized by the mean of the S_0 signal intensities (gray line) and that normalized by the extrapolated S_0 values from the spline fit (black line). C) Example z-spectra (black line, right y-axis) with Lorentzian fit (gray dashed line, right y-axis) used to calculate the APT_{Lor} (black arrow) and GAG_{Lor} (gray arrow) from the residuals of the fit (gray line, left y-axis).
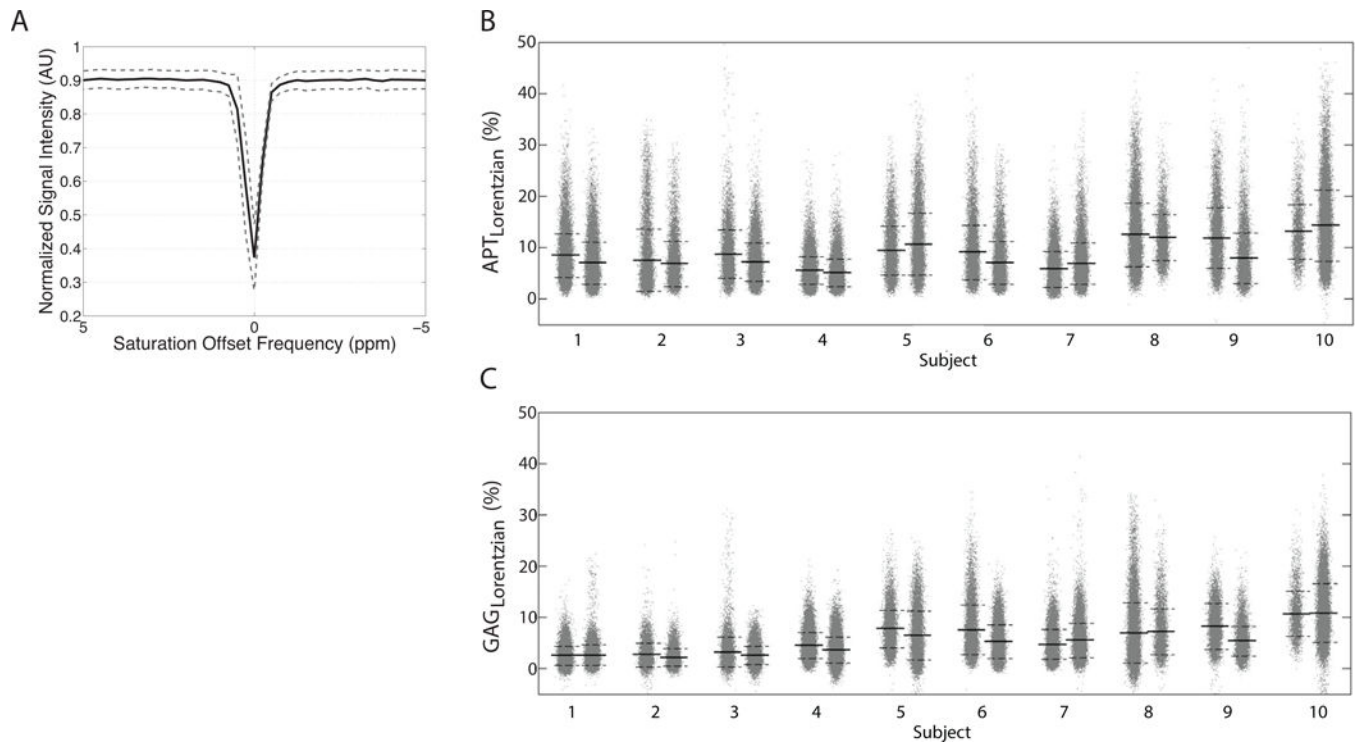
Figure 4.
Comprehensive CEST MRI results. A) The mean z-spectrum from masked FG tissue calculated for all 10 subjects is shown with the inter-scan standard deviation denoted by the dashed gray lines. Scan-rescan data are shown with each subjects' scans located adjacent to each other with the mean (solid black line) and standard deviation (dashed black lines) shown for the calculated B) APT_{Lor} and C) GAG_{Lor} metrics.
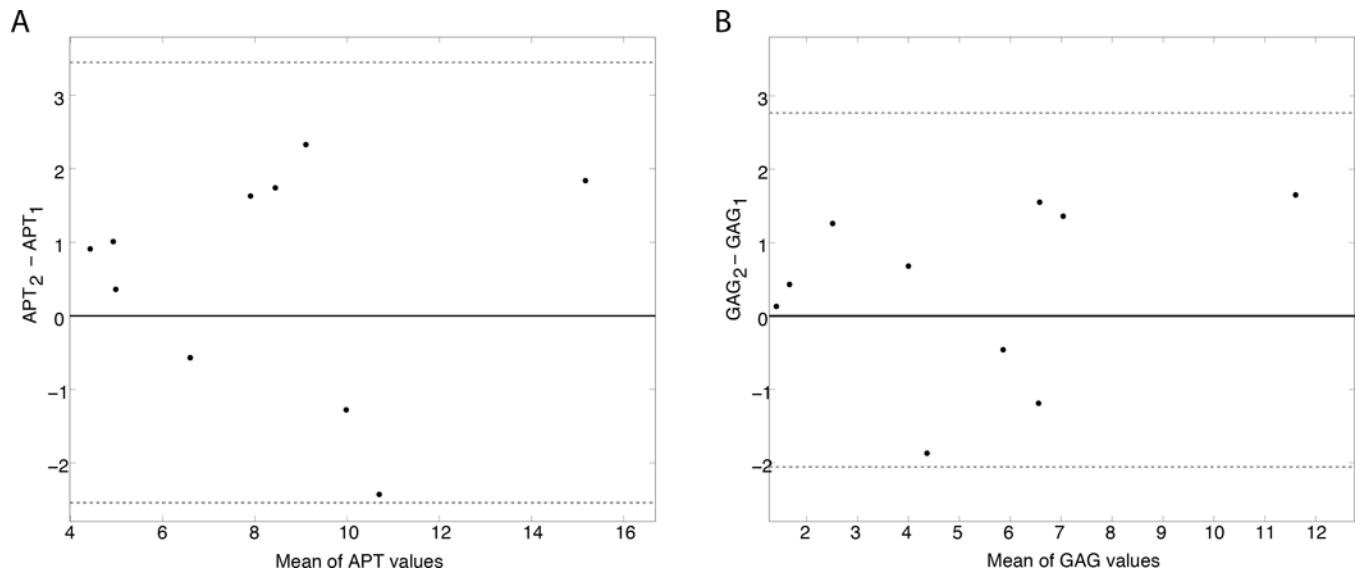
Figure 5.
Test-retest results for masked FG of ten healthy subjects. Bland-Altman plots for APT_{Lor} (Panel A) and GAG_{Lor} (Panel B) plot the difference between the mean scan values for each subject plotted against the mean of the respective CEST-derived metric. The mean difference values (black solid lines) and limits of agreement (dashed gray lines) are shown for both metrics.